

SOI by Smart-Cut. TEM-HRTEM Characterization of Structural Defects Induced in Si by Plasma Hydrogenation

Corneliu GHICA, Leona Cristina NISTOR

National Institute for Materials Physics, PO Box MG-7 Magurele, Bucharest, Romania
E-mail: cghica@infim.ro, leonis@infim.ro

Abstract. Silicon wafers have been submitted to hydrogen RF-plasma treatment in various experimental conditions. Three types of induced extended defects are identified and characterized by transmission electron microscopy: planar defects in the $\{111\}$ and $\{100\}$ planes and nanometric voids. The parameters of the plasma treatment have been varied in order to confine the induced defects in a 50 nm band below the surface. Laser treatment has been applied on the as-hydrogenated Si wafers. We will show laser annealing results in the formation of a well defined layer of nanometric cavities, favoring the peel off of a layer thinner than 50 nm.

1. Introduction

Silicon hydrogenation has a history of a few decades in the silicon industry. It has been intensively studied some decades ago as an important step in silicon technology. The role played by hydrogen atoms inserted in a silicon matrix, concerning the control of doping atoms activity, defect passivation or suppression of carrier traps, was evidenced and characterized [1-4]. Nowadays, silicon hydrogenation is studied in a new context, namely with the aim of developing and improving a technological method known as smart-cutTM used in the fabrication of 'silicon-on-insulator'(SOI) substrates [5]. The smart cut technique consists in creating a high density of crystal defects at a certain depth under the surface of a Si wafer, and then, to remove, by an appropriate method, the Si layer situated above the mechanically weakened region, which contains a high density of defects. The as-removed Si layer should remain single crystalline and, ideally, free of defects, in order to be used in a multilayer architecture of the kind 'single crystal layer / amorphous insulating layer / single crystal substrate'. The practical way used to induce crystal defects with a certain distribution profile under the Si wafer surface is either by ion implantation or by treatment in plasma of light atomic species, such as H or He [5-10]. Successful experiments have been reported concerning the smart-cut procedure by hydrogen ion implantation, where layers as thin as 200 nm have been removed from the Si wafers [5]. In our research we employ hydrogen

plasma in order to induce the necessary amount of defects. Apart from the lower cost, the use of H-plasma instead of H ion implantation could be, under appropriate conditions, less harmful for the Si layer to be removed by smart cut. Also, the possibility of peeling off even thinner layers is taken into consideration [11]. In general, the defects induced in Si by H ion implantation or H-plasma treatment, are planar defects, bubbles and dislocation loops [12, 13]. The high levels of H concentration in the Si lattice somehow complicate the problem, in the sense that the resulting defects are decorated with hydrogen and, therefore, different from the classical crystal defects encountered in Si. In order to be able to control the type of defects to be induced either by ion implantation or plasma treatment, the identification and characterization of defects in hydrogenated Si is necessary. This work contains qualitative and quantitative structural results obtained by conventional and high-resolution transmission electron microscopy (CTEM / HRTEM) on the defects in H-plasma treated Si wafers. We also present TEM results showing the evolution of the H-plasma induced structural defects in Si, in the case of surface laser annealing, with the aim to obtain a transferable single crystal Si layer thinner than 50 nm.

2. Experimental

p and *n*-type (001) Si wafers have been submitted to hydrogen RF-plasma treatments using a 13.56 MHz and a 110 MHz RF generator. The hydrogen partial pressure has been varied in the $10\text{-}10^4$ Pa range and the discharge power between 50-200W. The sample temperature did not exceed 200 °C during the treatment, the heating being caused by the interaction with the RF-plasma. The treatment duration varied from 1 h to 4 h. Transmission Electron Microscopy (TEM) investigations have been performed using the JEOL 200 CX and JEOL 4000 EX electron microscopes on specimens prepared by mechanical thinning and ion milling on a Gatan PIPS machine.

3. Results and Discussions

The effects of the hydrogen plasma treatment on the Si wafers may be immediately observed by TEM investigation on cross-section specimens. These effects can be summarized into two main categories: surface effects and subsurface effects. The surface effects consist in the appearance of a surface roughness due to the etching action of hydrogen plasma against Si. The subsurface effects consist in the formation of extended structural defects such as planar defects and nanocavities.

3.1. $\{111\}$ defects

The most frequently encountered defects in hydrogenated Si wafers are disposed along the $\{111\}$ planes. The slip system in Si is $\langle 110 \rangle \{111\}$, meaning that dislocations lie along the $\langle 110 \rangle$ directions and can slip across the dense $\{111\}$ planes. The typical example of a planar defect in materials with diamond structure is the stacking fault, resulting from the dissociation of a perfect dislocation into partials. However, the $\{111\}$ defects in the hydrogenated Si wafers show features

which make them different from the classical $\{111\}$ defects in materials having diamond structure.

Figure 1 reveals typical conventional TEM images of the $\{111\}$ defects encountered in the plasma hydrogenated Si samples. The bright field (BF) and dark field (DF)-images in Fig. 1 a and b, respectively, are obtained in Bragg condition with the 111 spot strongly excited.

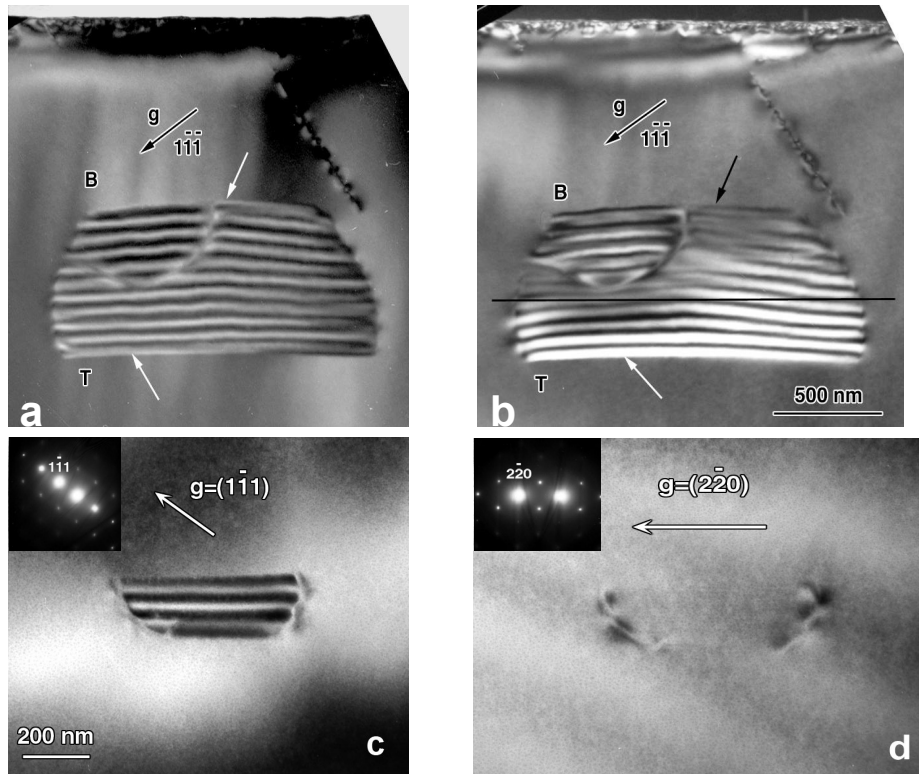


Fig. 1. Bright field (a) and dark field (b) images of a planar $\{111\}$ defect. ‘T’ and ‘B’ denote, respectively, the top and bottom ends of the planar defect intercepting the specimen surfaces. The black line on the DF image has been added as a reference in order to evidence the fringe curvature.

(c), (d) Bright field TEM images in Bragg condition of a $\{111\}$ planar defect using the 111 and 220 reflections.

Two $\{111\}$ defects can be observed. One of them, showing fringes, is buried at about 800 nm under the surface. By specimen tilting experiments, we have identified the habit plane for this defect as the (111) plane. The orientation of the reflection vector $g = (111)$ with respect to the bright outer fringe of the planar defect on the dark field image indicates that the defect has an intrinsic character,

i.e. has a missing silicon plane [14]. The second defect is seen in edge-on orientation. It is disposed in the $(\bar{1}\bar{1}\bar{1})$ plane and intercepts the wafer surface. As a typical feature for this kind of defects, the characteristic contrast fringes are not straight, but slightly curved, as can be noticed by comparison with the line drawn on figure 1b. It indicates that the defect is not limited to a single crystallographic plane, but it affects several adjacent planes.

Information about the displacement vector characterizing the $\{111\}$ planar defects can be extracted by imaging a defect in Bragg condition using the diffraction spots for which it becomes invisible. Two beam bright field images of such a defect are presented in figure 1 c and d, where the $\bar{1}\bar{1}\bar{1}$ and $\bar{2}\bar{2}\bar{0}$ reflections have been excited. The characteristic fringes of the defect became invisible for $\mathbf{g} = (\bar{2}\bar{2}\bar{0})$, showing that the characteristic displacement vector \mathbf{R} has no components along $[\bar{2}\bar{2}\bar{0}]$ and is most probably oriented perpendicular to the habit plane, as in the case of regular stacking faults [15].

In order to accede to the structure of defects at atomic level, HRTEM observations have been performed on $\{111\}$ defects in edge-on orientation. Figure 2 a shows the HRTEM image of a $\{111\}$ planar defect in the plasma hydrogenated silicon wafer, revealed in a very thin part of the specimen. Figure 2a shows a sharp contrast variation in the defect plane where the columns of atoms are revealed by a much brighter row of dots. In the centre of the figure the defect migrates over two adjacent $\{111\}$ planes leaving a jog behind. This fact explains the curvature and deformations of the fringes on the diffraction contrast images of the $\{111\}$ defects. In this situation, proposing a defect structure at atomic level is not an easy task. Several atomic models of the $\{111\}$ defects in hydrogenated silicon have been proposed, all of them taking into consideration the breaking of the Si-Si bonds along $\{111\}$ planes and the saturation of the resulting dangling bonds with hydrogen atoms, accompanied by longitudinal and/or transversal shifts of the Si lattice on each side of the defect. Atomic models proposed by Ponce et al. [16], Deák and Snyder [17], Van de Walle *et al.* [18], Zhang and Jackson [19], Heyman et al. [20] are summarized and simulated as HRTEM images by Muto et al. in [21].

To decide for a structural model of the $\{111\}$ defect in plasma hydrogenated Si, we processed the experimental HRTEM image of the $\{111\}$ defect to determine the strain field around the defect using the geometrical phase method (GPM) [22].

Figure 2 b gives the Fourier transform of the HRTEM image of the $\{111\}$ defect. An XY coordinate system has been chosen and indicated near the left low corner of the HR picture. The phase images in figures 2 c and d have been obtained by selecting with a Gaussian mask the $\bar{1}\bar{1}\bar{1}$ and $\bar{2}\bar{2}\bar{4}$ spots in figure 2 b, respectively. The local geometrical phase across the images is calculated with

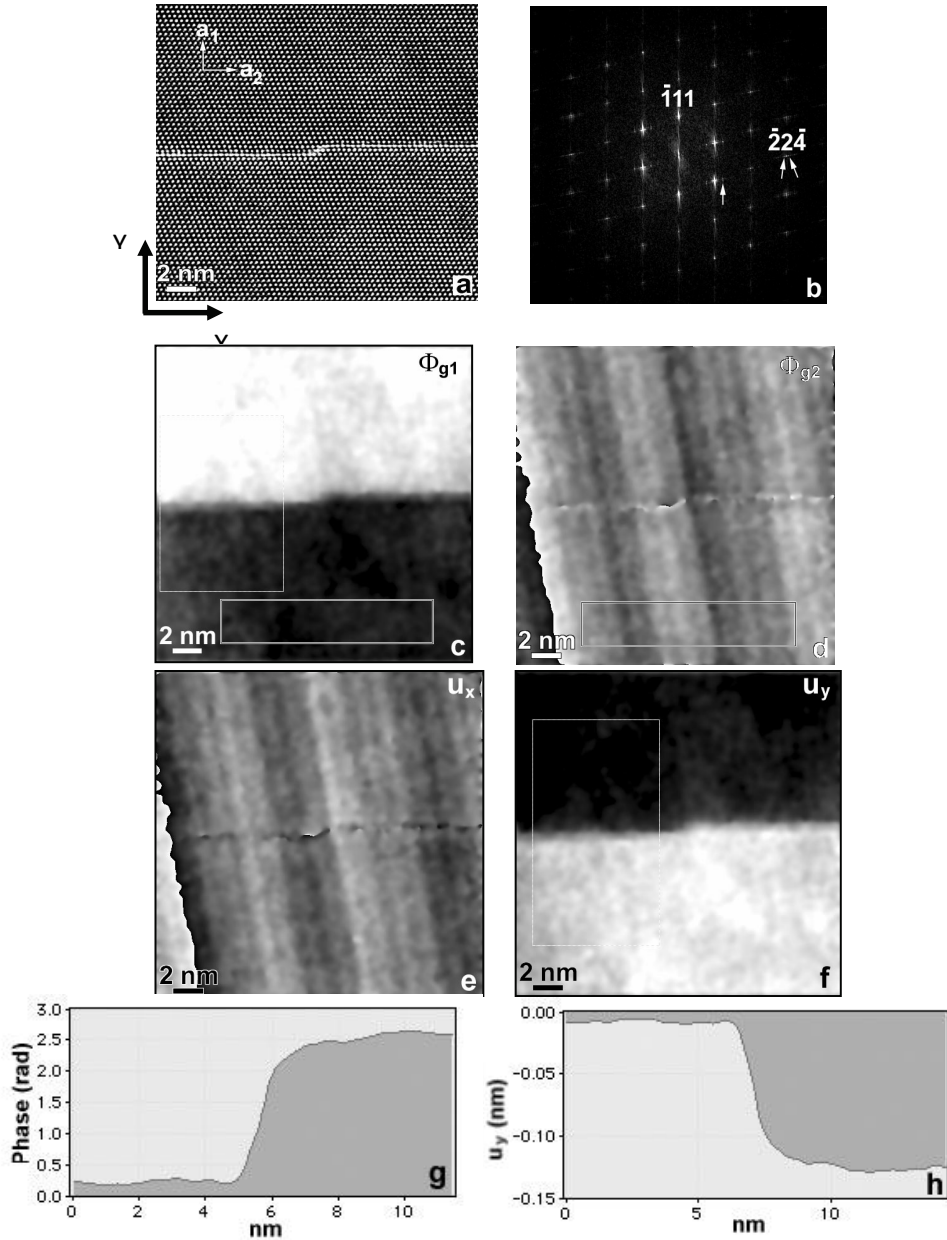


Fig. 2. (a) HRTEM image of the $\{111\}$ defect in the thin region; the assigned XY coordinate system is figured; (b) Fourier transform of the HRTEM image; (c), (d) Phase images Φ_{g1} and Φ_{g2} obtained by FFT^{-1} using a Gaussian mask around $g_1 = \bar{1}11$ and $g_2 = \bar{2}2\bar{4}$, respectively; (e), (f) $u_x(r)$ and $u_y(r)$ components of the displacement field $u(r)$ around the defect; (g) line profile of the phase across the defect in the Φ_{g1} phase image averaged over the 8 nm width of the rectangle in the left part of the image; (h) line profile of the $u_y(r)$ component across the defect in the positive sense of the OY axis.

respect to the average phase value corresponding to a reference area delimited by a rectangle in the low part of the phase images. On the phase images white / black areas correspond to regions of higher (positive) / lower (negative) phase, while grey areas are in phase (zero) with the reference area. One can notice on figure 2 c,

on the \mathbf{g}_1 phase image (Φ_{g1}), a clear phase jump of the $\bar{1}11$ fringes across the defect with respect to the reference area.

Using the two phase images, the displacement field $\mathbf{u}(\mathbf{r})$ can be calculated using the two real space vectors $\mathbf{a}_1 = 1/3 [\bar{1}11]$ and $\mathbf{a}_2 = 1/12 [\bar{1}1\bar{2}]$ corresponding to the reciprocal $\mathbf{g}_1 = [\bar{1}11]^*$ and $\mathbf{g}_2 = [\bar{2}24]^*$ vectors. The displacement field $\mathbf{u}(\mathbf{r})$ can be mapped by imaging its $u_x(\mathbf{r})$ and $u_y(\mathbf{r})$ components according to the equations:

$$\begin{aligned} u_x(\mathbf{r}) &= (-1/2\pi)[\Phi_{g1}(\mathbf{r})a_{1x} + \Phi_{g2}(\mathbf{r})a_{2x}] \\ u_y(\mathbf{r}) &= (-1/2\pi)[\Phi_{g1}(\mathbf{r})a_{1y} + \Phi_{g2}(\mathbf{r})a_{2y}] \end{aligned} \quad (1)$$

In our picture coordinate system $a_{1x} = 0$, $a_{1y} = |\mathbf{a}_1| = \sqrt{3}/3$ and $a_{2x} = |\mathbf{a}_2| = \sqrt{6}/12$, $a_{2y} = 0$, which turns equation (1) into:

$$\begin{aligned} u_x(\mathbf{r}) &= -(\sqrt{6}/24\pi)\Phi_{g2}(\mathbf{r}) \\ u_y(\mathbf{r}) &= -(\sqrt{3}/6\pi)\Phi_{g1}(\mathbf{r}) \end{aligned} \quad (2)$$

expressed in fractions of the lattice parameter, a , or:

$$\begin{aligned} u_x(\mathbf{r}) &= -0.176\Phi_{g2}(\mathbf{r}) \\ u_y(\mathbf{r}) &= -0.499\Phi_{g1}(\mathbf{r}) \end{aligned} \quad (3)$$

expressed in nm (the lattice parameter of Si is $a_{Si}=0.543$ nm).

The u_x and u_y components of the strain field calculated with (3) are depicted in figures 2 e and f where, again, grey means no displacement, white means positive displacement (in the positive sense of the coordinate axis) and dark means negative displacement. In figure 2 f one can notice a uniform negative rigid body displacement along OY (or $[\bar{1}11]$ direction) of the upper part of the image with respect to the reference area. The phase jump as well as the displacement field can be quantitatively expressed using line profiles across the defect.

Thus, the phase jump across the defect in the positive sense of the OY axis (Figure 2 g) measures $0.72\pi \pm 0.044$ radians. Correspondingly, the value of the u_y displacement measured on the line profile (Figure 2 h) is 0.116 ± 0.002 nm.

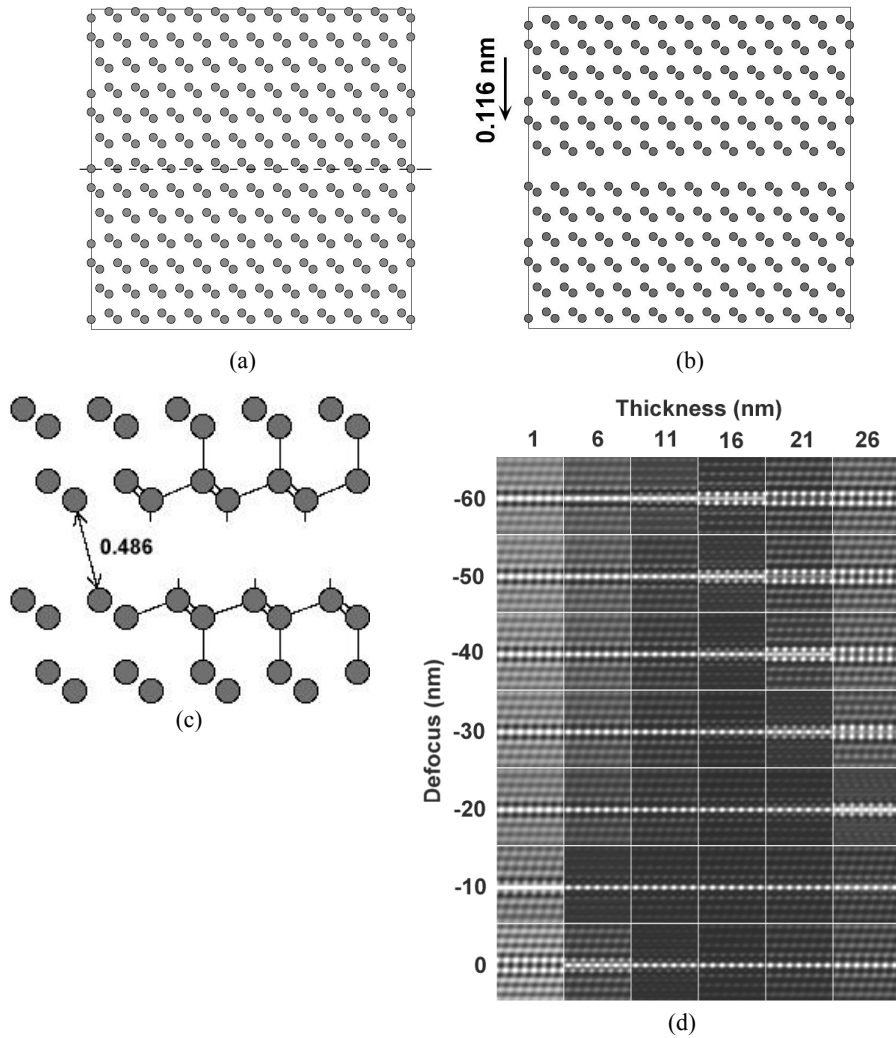


Fig. 3. Structural model of the $\{111\}$ defect based on the displacement values obtained by the GPM analysis. (a) Undistorted Si structure projected along $[110]$; the horizontal line marks the interface between the bottom fixed part of the crystal and the upper part which the displacement vector is applied to; (b) structural model *B* of the $\{111\}$ defect where two Si layers have been removed; (c) enlarged view of the atomic arrangement close to the defect plane for models *A* and *B*, respectively; interatomic distances in nm are indicated; (d) Matrix of simulated HR images for various thickness and defocus values based on the structural model (b).

We used the Crystal Kit software for the structural modelling of the defect. Starting from the undistorted Si crystal structure projected along $[110]$ (Figure 3 a), the 0.116 nm rigid body displacement has been applied to the upper part of the matrix with respect to the fixed bottom part, and two Si layers at the interface have

been removed (Figure 3 c). We consider that the resulting dangling bonds are saturated with hydrogen. A unit cell has been defined and simulated HR images have been calculated using the Mac Tempas software. In figures 3 d we present a series of simulated images obtained for different values for the lens defocus and specimen thickness. At a visual inspection of the simulated images we can conclude that the proposed structural model provides a perfect fit for the HR images of the defect. Thus, the defect is imaged as a single row of brighter dots in the thin areas of the specimen, as in the experimental image in figure 2 a.

3.2. $\{100\}$ defects

A second category of defects introduced by RF-plasma hydrogenation in silicon are the planar defects oriented along $\{100\}$ planes. In principle, $\{100\}$ planar defects are not encountered in diamond cubic materials, as $\{100\}$ is not a slip plane in these crystallographic systems. However, $\{100\}$ platelets have been reported for Si and Ge wafers submitted to deuteron irradiation [23, 24].

As in the case of the $\{111\}$ defects, the interpretation of the HRTEM images of the $\{100\}$ defects in hydrogenated Si wafers is rather difficult due to the presence of a high strain field around them. Moreover, unlike the $\{111\}$ defects, the $\{001\}$ defects proved to be rather unstable when imaged at 400 kV in HR conditions. Therefore, special precautions have been taken in order to record the HR images, such as performing the fine imaging adjustments on a different thin area away from the defect and, especially, working fast by taking HRTEM images within the first 20 seconds of defect imaging. It is well known that for accelerating voltages higher than 300 kV, the electron beam creates defects in Si by a knock-off mechanism. We noticed this effect in our specimens during observation in HR conditions at 400 kV. However, while the $\{111\}$ defects were not beam sensitive, the $\{001\}$ defects disappeared after about 20 seconds of observation in HR conditions at 400 kV and the Si matrix was healed.

A fragment from the central region of such a defect in edge-on orientation is imaged in Figure 4 a. The defect is not limited to a single crystallographic plane. It has a diffuse aspect affecting two or three neighboring (001) planes. Like the $\{111\}$ defects, it migrates to adjacent planes, which gives it a slightly curved lens-like shape. Fourier filtered images obtained by selecting the $\bar{1}11$ and 002 spots from the power spectrum (Figure 4 b) are displayed in Figures 4 c and d, respectively.

The $(\bar{1}11)$ family of planes is only weakly affected by the presence of the defect and the corresponding Fourier-filtered image has not been included here. However, for the $(\bar{1}11)$ planes, a phase shift can be observed in the upper part of the image with respect to the bottom part across the defect (Figure 4 c).

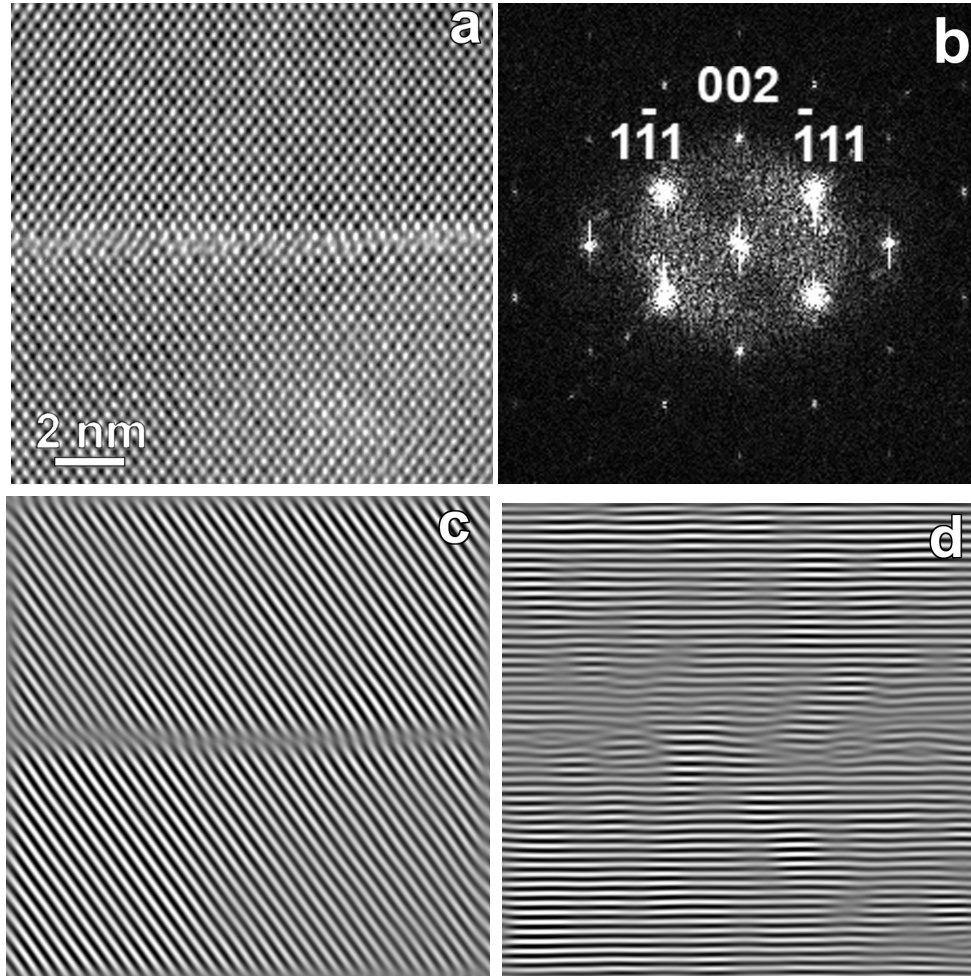


Fig. 4. (a) HRTEM image of an (001) defect; (b) the corresponding power spectrum; (c), (d) Fourier filtered images showing the (111) and (002) planes, respectively.

The 002 filtered image (Figure 4 d) shows important distortions especially along the defect, where fragments of interstitial (002) planes can be observed. The defect has not a unique extrinsic or intrinsic character, but rather a mixed one, resulting probably from accumulation of vacancies and self-interstitials followed by their condensation on a $\{001\}$ plane, as revealed by the 002 filtered image. It is well known in literature that this mechanism represents the way in which prismatic dislocation loops are formed [25]. The loss of fringe contrast can be related to a high degree of disorder in the lattice. Since this kind of defect is not characteristic

to silicon, but it occurs only in hydrogenated wafers, one could infer that the vacancies and interstitials involved are generated from the interaction between the Si lattice and the in-diffused H atoms.

3.3. Nano-cavities

From previous observations on He implanted silicon [26], bubbles were expected to appear in hydrogenated Si, as well. However, TEM observations revealed their rather seldom presence both in plan-view and cross-section specimens. In general, they appear as agglomerations of bubbles around 5-20 nm in size and they are surrounded by long range strain field; when imaged in plan-view close to the [001] zone axis, a 4-fold symmetry contrast surrounds them. In order to elucidate the origin of this contrast, we have performed tilting and defocus variation experiments.

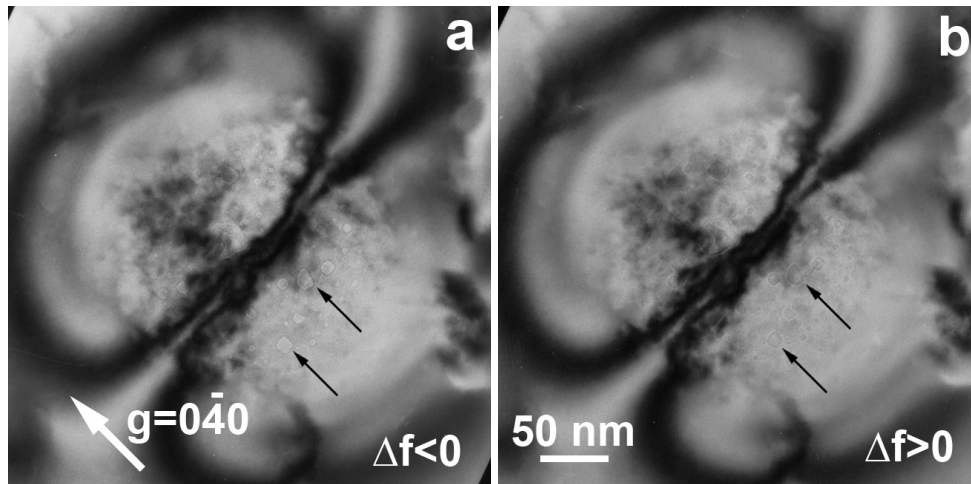


Fig. 5. TEM images on a plan-view specimen showing the strain field contrast around the defect in two-beam condition ($0\bar{4}0$ reflection excited): under focused (a) and over focused (b) images showing nanometric bubbles with, respectively, bright and dark inner fringe contrast.

Figure 5 shows two-beam images of the defect, $\mathbf{g}=(0\bar{4}0)$, in a plan-view specimen prepared from a hydrogenated Si(001) wafer. The two images present a bubble agglomeration surrounded by a 2-lobed strain field contour. The nature of the defect can be resolved on over focused ($\Delta f > 0$) and under focused ($\Delta f < 0$) images. For negative defocus the bubbles show a bright inner fringe, while for positive defocus the inner fringe becomes dark. This contrast behavior is characteristic for cavities inside a solid matrix [27]. The formation mechanism seems to be the same as in the case of the $\{001\}$ defects, namely an accumulation

of in-excess vacancies. The interaction between the in-diffused H atoms and the Si lattice, based on the high chemical reactivity of the H atoms against the Si-Si bonds, is at the origin of the lattice vacancies and self-interstitials formation. These agglomerations of nano-cavities are always surrounded by long-range strain-field contours, demonstrating that high mechanical tensions are concentrated here.

3.4. Plasma treatment optimization

Si{001} wafers have been submitted to hydrogen RF-plasma treatment in optimized experimental conditions in order to avoid roughness increase and to create a thin subsurface layer (50 nm thin or less) containing a high density of structural defects [28]. The hydrogen RF-plasma has been created inside a discharge chamber between two flat electrodes separated at adjustable distance, with the Si wafer between the two electrodes. We have used two parallel disk-shaped electrodes with a diameter of 30 mm, separated at a distance of 30 mm. One of the two electrodes was grounded, while the RF signal with a power of 50 W or 200 W at 13.56 MHz was applied on the second electrode. The value of the hydrogen dynamical pressure inside the chamber was set in the 7.5–55 Pa range using a hydrogen flow of 10–20 sccm. The Si wafers were mounted on the grounded electrode and the treatment duration was 1 h. The temperature of the Si wafers during the treatment was less than 250°C, the increase from room temperature being due to the plasma bombardment.

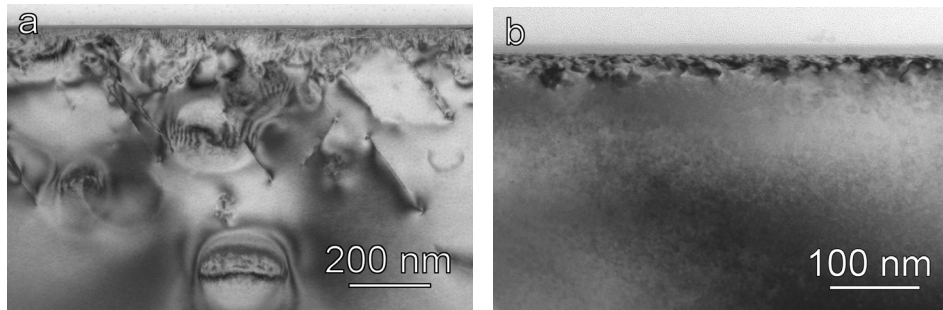


Fig. 6. Cross-section TEM images of Si wafers treated in hydrogen RF-plasma showing the extent of the defect-containing region as a function of the RF-discharge power: 200 W in (a) and 50 W in (b).

Figure 6 shows the cross-section TEM image of as-hydrogenated Si(001) wafers treated in the RF plasma at 50 W and 200 W. Two surface-related features of the as-hydrogenated sample are noticeable: i. a thin amorphous layer on the surface; ii. the roughness of the crystalline Si surface is of the order of the nanometer (peak-to-valley amplitude). Investigating samples treated at different plasma power values, we have noticed that the thickness of the amorphous surface layer after the RF-plasma treatment diminishes by increasing the RF-plasma power, from ca. 15 nm for the RF-plasma at 50 W down to 10 nm or thinner for

plasma treatment at 100 W and 200 W. Regarding the origin and history of this amorphous layer, we believe that it comes from the native SiO₂ layer on top of the Si wafer which has been chemically reduced to Si during the H-plasma treatment and then re-oxidized, once exposed to the air. In addition, the diminishing of its thickness with the increase of the plasma power is caused by the etching effect of hydrogen plasma, being more effective in the case of more energetic plasmas. Therefore, the presence of this thin SiO₂ layer on top of the hydrogen-containing Si single crystal characterizes the initial state of surface for the as-hydrogenated Si wafers when further submitted to thermal treatment or laser annealing. From the point of view of the final SOI architecture, we consider that the presence of this amorphous SiO₂ layer does not represent a major drawback, since the peeled-off layer will include a Si layer with a thin SiO₂ layer on top of it and the target substrate will be also a SiO₂-terminated Si wafer.

Below the surface, one can notice a region with a high density of structural defects. Most of the defects are planar defects situated in the {111} and {001} crystallographic planes. The extent of this faulted region is strongly dependent on the power of the RF discharge during the plasma treatment. It decreases from almost 1 μm in the case of the 200 W RF plasma (Figure 6 a) down to about 50 nm for the 50 W RF plasma (Figure 6 b). The high density of structural defects concentrates a significant strain field which can be noticed as a strong dark diffraction contrast. The structural defects induced by the hydrogen plasma treatment represent a straightforward indication regarding the depth range where hydrogen is present in a significant quantity.

3.5. Laser annealing

The difficulty posed by the plasma treatment in comparison with the ion implantation regarding the induced defects is that, in the case of plasma treatment, the induced defects intercept the wafer free surface. This does not occur for the ion implantation where the damaged layer is buried at a certain depth under the implanted surface, well separated from it. Therefore, in the case of plasma-hydrogenated wafers, where the defected region is adjacent to the surface, the after-hydrogenation treatment should result in a clear separation between the defect-containing region and the surface. The obtained defect configuration would be, this way, similar to the implanted samples, with the possibility to peel-off layers thinner than 50 nm. Several attempts to obtain such a result by classical thermal treatments of the plasma hydrogenated Si wafers failed, because, especially the {111}-type defects, which might intersect the wafer surface, are not annealed out. Therefore, we proposed to study laser annealing as an alternative method of after-hydrogenation treatment. The very principle of the laser annealing differs fundamentally from the thermal annealing. As in the case of any surface treatment using various energy sources, the energy transfer towards the material occurs

through the exposed surface. Depending on the experimental parameters, the energy transfer may be restricted to a narrow region of material in the surface vicinity, as opposed to classical thermal annealing which affects the whole volume of the sample.

In the case of our laser annealing experiments we used as irradiation laser beam the 3-rd harmonic $\lambda=355$ nm, corresponding to 3.49 eV photon energy, from a YAG:Nd source ($\lambda=1.06$ μm). At this wavelength, the optical absorption coefficient of Si is ca. 10^6 cm^{-1} [29]. From the Beer-Lambert law of radiation absorption, $I(x)=I_0\exp(-\alpha x)$, where α is the optical absorption coefficient, applied to a Si wafer under 355 nm laser radiation, it turns out that 90% of the absorbed incident beam energy (after subtracting the reflected beam) is confined to the first 23 nm of material. This preliminary information attests the fact that laser annealing offers the premises to concentrate a high density of energy into a very thin layer of Si with a thickness comparable or even less than that of the defect-containing layer after hydrogenation. In case the amount of laser energy deposited into the first 23 nm is enough to heal the defects encountered in this region, then the laser annealed sample would contain a certain density of defects embedded under a very thin (ca. 20 nm) layer of defect-free Si, which is exactly the desired distribution of structural defects needed for the smart-cut procedure. For our laser annealing experiments, the laser fluence on the surface of the as-hydrogenated wafers was 0.15 J/cm^2 , with the laser beam spread over an area of ca. 1 cm^2 . This fluence value is an order of magnitude below the ablation threshold of Si, reported to be around 1.8 J/cm^2 [30, 31].

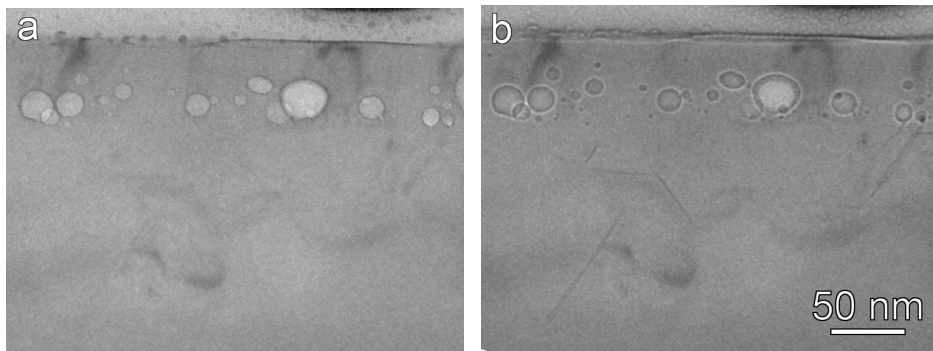


Fig. 7. Cross-section TEM images at low-magnification of a Si wafer after hydrogenation in RF-plasma at 200 W and subsequent pulsed laser annealing, for $\Delta f < 0$ (a) and $\Delta f > 0$ (b).

The consequences of the laser treatment on the surface of the Si wafer hydrogenated at 200 W can be immediately noticed in Figure 7. One can see that some of the planar defects are still present, in a region running deep (ca. 800 nm) under the treated surface, while the region close to wafer surface is defect free.

However, in addition to the hydrogen induced defects, a string of circular features right below the surface becomes visible after the laser treatment.

The nature of these features is rapidly identified in electron microscopy by comparing pairs of images obtained under opposite objective lens defocus conditions, meaning underfocused image ($\Delta f < 0$) and overfocused image ($\Delta f > 0$). By comparing the two underfocused and overfocused images, it becomes clear that the effect of the laser annealing is the formation of nanometric cavities with sizes ranging from 5-6 nm up to 50-60 nm. It is interesting to note that these nanocavities are distributed at a high density within a narrow layer of material (about 50 nm thick) below the surface. It is important to observe, also, that there is an even narrower layer of material (about 35 nm thick), between the free surface and the string of nanocavities, which contains no nanocavities at all. The concentration of the laser-formed nanocavities in a narrow band below the surface determines the mechanical weakening of the Si matrix in that region and creates the premises to lift off layers thinner than 50 nm.

4. Conclusions

Our work has demonstrated that laser annealing of RF-plasma hydrogenated Si wafers represents a reliable method of inducing appropriated structural defects in terms of density and spatial distribution for the subsequent removal of thin layers by the smart-cut procedure. The method combines RF-plasma treatment and UV laser annealing, which are sensibly cheaper than other techniques employed so far, such as ion implantation or molecular beam epitaxy. Hydrogen diffusion into the Si structure during the treatment in the RF-plasma is accompanied by the formation of extended structural defects (mostly $\{111\}$ and $\{100\}$ planar defects) and surface corrugation. The amplitude of these effects as well as the hydrogen quantity inside the Si matrix may be controlled through the experimental parameters such as set-up geometry, discharge power, etc. Pulsed laser annealing has been applied to as-hydrogenated Si wafers using the 3-rd harmonic of a YAG:Nd laser source. The rapid absorption of the UV laser radiation into the first tens of nm of Si results in the formation of a well defined layer of nanometric voids placed at a depth of 25-50 nm, depending on the experimental conditions. The highly populated layer of laser induced nanocavities determines an increased structural fragility of the Si matrix favoring the smart-cut process. These results are highly encouraging in considering RF-plasma treatment corroborated with laser annealing as an alternative reliable method to induce structural defects in a controllable manner below the surface of a Si wafer and to favor the peel off by smart-cut of Si layers thinner than 50 nm. For further understanding the mechanism of the nanocavity generation by vacancy diffusion under the thermal gradient induced by the laser treatment, the calculation of the temperature field inside the Si target in function of the laser beam parameters (wavelength, fluence, power, repetition rate, number of

shots) corroborated with the vacancy transient diffusion process will be performed as future work.

Acknowledgements. This work has been partially supported by CNCSIS in the frame of the national research program PN II Ideas (Contract No. 233/2007).

References

- [1] PANKOVE J.I., CARLSON D.E., BERKEYHEISER J.E., WANCE R.O., Phys. Rev. Lett. **51**, p. 2224, 1983.
- [2] JOHNSON N.M., Phys. Rev. B **31**, p. 5525, 1985.
- [3] JOHNSON N.M., HAHN S.K., Appl. Phys. Lett. **48**, p. 709, 1986.
- [4] SPEAR W.E., LeCOMBER P.G., Solid State Comm. **17**, p. 1193, 1975.
- [5] BRUEL M., Nucl. Instr. and Meth. in Phys. Reas. B **108**, p. 313, 1996.
- [6] JOHNSON N.M., PONCE F.A., STREET R.A., NEMANICH R.J., Phys. Rev. B **35**, p. 4166, 1987.
- [7] JENG S.J., OEHRLEIN G.S., SCILLA G.J., Appl. Phys. Lett. **53**, p. 1735, 1988.
- [8] RANGAN S., ASHOK S., CHEN G., THEODORE D., Nucl. Instr. and Meth. in Phys. Reas. B **206**, p. 417, 2003.
- [9] QIAN C., TERREAULT B., GUJRATHI S.C., Nucl. Instr. and Meth. in Phys. Reas. B **175-177**, p. 711, 2001.
- [10] FICHTNER P.F.P., KASCHNY J.R., BEHAR M., YANKOV R.A., MÜCKLICH A., SKORUPA W., Nucl. Instr. and Meth. in Phys. Reas. B **148**, p. 329, 1999.
- [11] USHENKO A.Y., ULYASHIN A.G., Jpn. J. Appl. Phys. **41**, p. 5021, 2002.
- [12] GHICA C., NISTOR L.C., BENDER H., RICHARD O., TENDELOO Van G., ULYASHIN A., Phil. Mag. **86**, p. 5137, 2006.
- [13] GHICA C., NISTOR L.C., BENDER H., RICHARD O., TENDELOO Van G., ULYASHIN A., J. Phys. D: Appl. Phys. **40**, p. 395, 2007.
- [14] SAADA G., *Microscopie électronique des lames minces cristallines* (Masson & C^{ie}, Paris, pp. 235–237, 1966.
- [15] HIRSCH P.B., HOWIE A., NICHOLSON R.B., PASHLEY D.W., WHELAN M.J., *Electron Microscopy of Thin Crystals*, Butterworth & Co., pp. 165, London, 1967.
- [16] PONCE F.A., JOHNSON N.M., TRAMONTANA J.C., WALKER J., Inst. Phys. Conf. Ser. **87**, p. 49, 1987.
- [17] DEÁK P., SNYDER L.C., Radiat. Effects **111-112**, p. 77, 1989.
- [18] WALLE De Van C.G., DENTENEER P.J.H., BAR-YAM Y., PANTELIDES S., Phys. Rev. Lett. **60**, p. 2761, 1989.
- [19] ZHANG S.B., JACKSON W.B., Phys. Rev. B **43**, p. 12142, 1991.
- [20] HEYMAN J.N., AGER III J.W., HALLER E.E., JOHNSON N.M., WALKER J., DOLAND C.M., Phys. Rev. B **45**, p. 13363, 1992.
- [21] MUTO S., TAKEDA S., HIRATA M., Phil. Mag. A **72**, p. 1057, 1995.
- [22] HÛTCH M.J., SNOECK E., KILAAS R., Ultramicroscopy **74**, p. 131, 1998.
- [23] MUTO S., TAKEDA S., Phil. Mag. Lett. **72**, 99, 1995.
- [24] AKATSU T., BOURDELLE K.K., RICHTARCH C., FAURE B., LETERTRE F., Appl. Phys. Lett. **86**, p. 181910, 2005.
- [25] HULL D., *Introduction to Dislocations*, 2nd edition, Oxford: Pergamon 1975.
- [26] CEROFOLINI G.F., CORNI F., FRABNONI S., NOBILI C., OTTAVIANI G., TONINI R., Mat. Sci. Eng. **27**, p. 1, 2000.
- [27] WILLIAMS D., CARTER C.B., *Transmission Electron Microscopy*, **3**, New York and London: Plenum 1996.

- [28] GHICA C., NISTOR L.C., VIZIREANU S., DINESCU G., MOLDOVAN A., DINESCU M., Plasma Proc. Polym. **7**, p. 986, 2010.
- [29] JELLISON Jr.G.E., MODINE F.A., J. Appl. Phys. **53**, p. 3745, 1982.
- [30] WAKATA H., TASEV E., TUDA M., ONO K., HARUTA K., and UEDA Y., Appl. Surf. Sci. **79-80**, p. 152, 1994.
- [31] TORRISI L., BORRIELLI A., and MARGARONE D., Nucl. Instr. Meth. B **255**, p. 373, 2007.